A bifurcation study of mixed-convection heat transfer in horizontal ducts

By K. NANDAKUMAR[1] AND H. J. WEINITSCHKE[2]

[1] Department of Chemical Engineering, University of Alberta, Edmonton, Alberta, Canada T6G 2G6

[2] Institut für Angewandte Mathematik, Universität Erlangen – Nürnberg, 8520 Erlangen, Federal Republic of Germany

The bifurcation structure of two-dimensional, pressure-driven flows through a horizontal, rectangular duct that is heated with a uniform flux in the axial direction and a uniform temperature around the periphery is examined. The solution structure of the flow in a square duct is determined for Grashof numbers (Gr) in the range of 0 to 10^6 using an arclength continuation scheme. The structure is much more complicated than reported earlier by Nandakumar, Masliyah & Law (1985). The primary branch with two limit points and a hysteresis behaviour between the two- and four-cell flow structure that was computed by Nandakumar *et al.* is confirmed. An additional symmetric solution branch, which is disconnected from the primary branch (or rather connected via an asymmetric solution branch), is found. This has a two-cell flow structure at one end, a four-cell flow structure at the other, and three limit points are located on the path. Two asymmetric solution branches emanating from symmetry-breaking bifurcation points are also found for a square duct. Thus a much richer solution structure is found with up to five solutions over certain ranges of Gr. A determination of linear stability indicates that all two-dimensional solutions develop some form of unstable mode by the time Gr is increased to about 220000. In particular, the four-cell becomes unstable to asymmetric perturbations. The paths of the singular points are tracked with respect to variation in the aspect ratio using the fold-following algorithm. Transcritical points are found at aspect ratios of 1.408 and 1.456 respectively for Prandtl numbers $Pr = 0.73$ and 5. Above these aspect ratios the four-cell solution is no longer on the primary branch. Some of the fold curves are connected in such a way as to form a tilted cusp. When the channel cross-section is tilted even slightly (1°) with respect to the gravity vector, the bifurcation points unfold and the two-cell solution evolves smoothly as the Grashof number is increased. The four-cell solutions then become genuinely disconnected from the primary branch. The uniqueness range in Grashof number increases with increasing tilt, decreasing aspect ratio and decreasing Prandtl number.

1. Introduction

Mixed-convection heat transfer in horizontal ducts has been studied quite extensively since the early work of Morton (1959). Interest in the mixed-convection problem stems in part from the importance of such mechanisms in heat exchangers. A forced flow is maintained through the duct by an imposed pressure gradient, $\mathrm{d}p'/\mathrm{d}z'$. Although several alternative means of heating are possible, we consider the case examined by Morton (1959) viz. an axially uniform heat flux condition realizable

by electrical heating. Furthermore we consider the case of fully developed (a term used synonymously with two-dimensional, and axially invariant) flow conditions such that the bulk temperature of the fluid increases linearly in the axial direction, i.e. $dT_b''/dz' = $ constant. Morton (1959) studied the flow in a circular geometry and treated the buoyancy effect as a perturbation over the Poiseuille flow. He developed a three-term, regular series expansion following essentially Dean's (1927) development of a similar series solution for flow in a curved duct. Since that time the similarity between the buoyancy-driven secondary flow in the mixed-convection problem and the centrifugal force-driven secondary flow in the Dean problem has been recognized by a number of investigators. In recent years an equally important motivating factor for studying these two problems has been the hydrodynamic stability and bifurcation aspects of the flow. Winters (1987) has presented the most comprehensive bifurcation study of the Dean problem in curved ducts of rectangular cross-section. Dennis & Ng (1982), Nandakumar & Masliyah (1982) and Yang & Keller (1986a) have examined similar aspects in curved ducts of circular cross-sections.

The early theoretical work using a perturbation approach by Morton (1959), Iqbal & Stachiewicz (1966) and Faris & Viskanta (1969) marked the beginnings of a rational analysis of the mixed-convection problem. The numerical study of the problem by Cheng & Hwang (1969) and Hwang & Cheng (1970) was limited to a Gr of about 50000 and only a two-cell pattern was observed over this range. The most recent work is by Van Dyke (1990) who has used the computer-extended Stokes series to elucidate the flow structure at large values of the dynamical parameter. The questions regarding bifurcation have been left unresolved. The earliest evidence of a transition to a four-cell flow structure was contained in the numerical work by Patankar, Ramadhyani & Sparrow (1978) who examined the effect of non-uniform peripheral heating in a duct of circular cross-section. A similar transition was observed by Chou & Hwang (1984) for a rectangular geometry with uniform heating. Multiplicity, however, was not demonstrated in any of these works. Nandakumar, Masliyah & Law (1985, hereinafter referred to as I) demonstrated that multiple, two-dimensional solutions exist for this problem in ducts of square, circular and semicircular cross-sections. More complete references to other experimental and numerical work on mixed convection can be found in (I). Here we review the known aspects of the flow structure and compare it with that of the Dean problem.

The dynamical parameters in the Dean and mixed-convection problems are, respectively, the Dean number $(Dn = Re/R_c^{\frac{1}{2}})$ and the Grashof number $(Gr = a^3\beta gQ'/kv^2)$. Here Re is the Reynolds number, R_c is the radius of curvature of a curved duct, a is half the channel height, β is the coefficient of thermal expansion for the fluid, g is the acceleration due to gravity, Q' is the heat transfer rate per unit length of the duct, k is the thermal conductivity of the fluid and v is the kinematic viscosity. In both problems, a typical two-dimensional flow structure at sufficiently small values of the dynamical parameter consists of two counter-rotating vortices in a plane perpendicular to the axis of the duct. The interaction of the secondary flow with the pressure-driven primary flow causes a shift in the location of the maximum axial velocity away from the centre of the duct and in the direction of the secondary velocities in the middle of the channel. Upon increasing the value of the dynamical parameter sufficiently, the two-cell flow structure becomes unstable and gives way to another form of two-dimensional flow with a four-cell structure in the cross-plane. Winters (1987) found such four-cell flows in the Dean problem to be unstable to asymmetric perturbations. Similar results are found in the present work on the
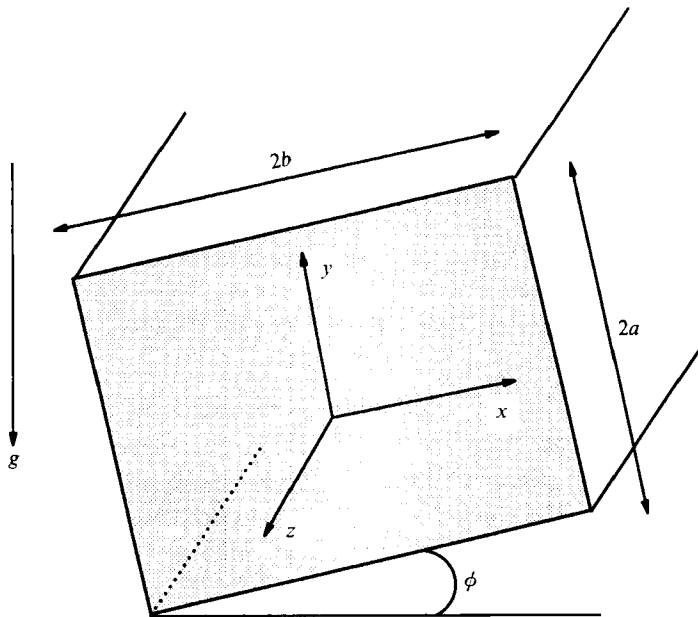
FIGURE 1. Geometry and coordinate system.

mixed-convection problem. Upon increasing the dynamical parameter even more, all two-dimensional flows become unstable, and there is evidence for the evolution of streamwise periodic three-dimensional flows in both the problems (Ravi Sankar, Nandakumar & Masliyah 1988; Ravi Sankar, Nandakumar & Weinitschke 1991). The three-dimensional flow structure of the mixed convection problem will be presented in a follow-up study.

The present work is confined to a study of two-dimensional flows and extends the results presented in (I) in several ways. Certain mean-square estimates, which can be useful in developing uniqueness proofs, are presented in §3. The numerical methods are outlined in §4. The slowly convergent successive relaxation scheme used in (I) is replaced by the more effective Euler–Newton continuation scheme. Unlike in (I) the reflective symmetry is not imposed and both symmetric and asymmetric solutions are sought by solving over appropriate flow domains. The limit points were bracketed in (I) using the simple bisection algorithm. In the present work both the limit points and symmetry-breaking bifurcation points are determined precisely using the extended system formulations of Moore & Spence (1980), Spence & Werner (1982) and Werner & Spence (1984). In addition, using the tilt of the channel cross-section, ϕ, with respect to the gravity vector (see figure 1) as a new unfolding parameter, together with the pseudoarclength continuation method proposed by Keller (1977), several additional solution branches are discovered. More specifically, for $Pr = 0.73$ in a square duct, the primary branch with two limit points that was computed in (I) is confirmed. In addition, a new isolated symmetric branch and two new asymmetric solution branches which emanate from symmetry-breaking bifurcation points are discovered within a Grashof number range of 0 to 10^6.

Next the variation of these singular points with aspect ratio, $\gamma = b/a$ (where $2b$ is the channel width) is tracked for the case of zero tilt with the fold-following algorithm for two Prandtl numbers of 0.73 and 5.0. Higher-order singularities are present on these fold curves, but their locations are only bracketed approximately.

For a square duct, the variation of these singular points with the Prandtl number is also tracked over a range of 0.73 to 5.0 which are typical values for air and water, respectively. No higher-order singularities are found on these folds. The linear stability of the various solution branches for a square duct is determined using a combination of power iteration and eigenvalue calculations. As there is no method of predicting *a priori* the total number of solutions for a given parameter set, one cannot be certain that all the two-dimensional solution branches of interest have yet been discovered. However, a self-consistent picture of the solution structure emerges from this study. Several features of the solution structure are found to be quite similar to those observed by Winters (1987) for the Dean problem and also to a convective heat transfer problem in porous media studied by Weinitschke *et al.* (1990).

2. Governing equations

A rectangular duct of width $2b$ and height $2a$ is considered. The aspect ratio of the duct is $\gamma = b/a$. The axis of the duct is aligned perpendicular to the gravity vector. The cross-section of the duct can be tilted by ϕ° with respect to the gravity vector as shown in figure 1. The flow is driven by a constant imposed pressure gradient, dp'/dz' and heated by an axially uniform flux, dT'_b/dz'. Thus an axially invariant state is assumed to exist, namely $v' = (u'(x,y), v'(x,y), w'(x,y))$. Furthermore, the Boussinesq approximation is invoked to account for the density variation, $\rho = \rho_r[1 - \beta(T' - T'_r)]$, only in the buoyancy force term, g. Here the subscript r denotes a reference state. The equations of motion subject to these conditions are:
continuity

$$\frac{\partial u'}{\partial x'} + \frac{\partial v'}{\partial y'} = 0; \tag{1}$$

x-momentum

$$\frac{\partial u'}{\partial t'} + \left(u'\frac{\partial u'}{\partial x'} + v'\frac{\partial u'}{\partial y'}\right) = -\frac{1}{\rho_r}\frac{\partial p'}{\partial x'} + \nu'\nabla^{2'}u' - \frac{\rho g}{\rho_r}\sin\phi; \tag{2}$$

y-momentum

$$\frac{\partial v'}{\partial t'} + \left(u'\frac{\partial v'}{\partial x'} + v'\frac{\partial v'}{\partial y'}\right) = -\frac{1}{\rho_r}\frac{\partial p'}{\partial y'} + \nu'\nabla^{2'}v' - \frac{\rho g}{\rho_r}\cos\phi; \tag{3}$$

z-momentum

$$\frac{\partial w'}{\partial t'} + \left(u'\frac{\partial w'}{\partial x'} + v'\frac{\partial w'}{\partial y'}\right) = -\frac{1}{\rho_r}\frac{\partial p'}{\partial z'} + \nu'\nabla^{2'}w'; \tag{4}$$

energy equation

$$\frac{\partial T'}{\partial t'} + \left(u'\frac{\partial T'}{\partial x'} + v'\frac{\partial T'}{\partial y'} + w'\frac{\partial T'}{\partial z'}\right) = \alpha\nabla^{2'}T'. \tag{5}$$

Note that a fully developed state implies, $\partial T'/\partial z' = dT'_b/dz'$. Since the flow is two-dimensional, the stream function, ψ', and the axial vorticity, Ω' can be introduced as

$$u' = \frac{\partial \psi'}{\partial y'}, \quad v' = -\frac{\partial \psi'}{\partial x'}, \quad \Omega' = \frac{\partial v'}{\partial x'} - \frac{\partial u'}{\partial y'}. \tag{6}$$

Equations (1)–(5) are then cast in the standard stream function–vorticity formulation as in (I). The following scales are used to normalize the variables:

$$x = \frac{x'}{b}, \quad y = \frac{y'}{a}, \quad \tau = \frac{t'}{a^2/\nu}, \quad u = \frac{u'}{\nu/a}, \quad v = \frac{v'}{\nu/b}, \quad w = \frac{w'}{(-dp'/dz')a^2/\rho\nu)},$$

$$\psi = \frac{\psi'}{\nu}, \quad \Omega = \frac{\Omega'}{\nu/a^2}, \quad \theta = \frac{T_w' - T'}{(dT_b'/dz')(-dp'/dz')a^4/\rho\nu^2},$$

where T_w' is the wall temperature. The dimensionless form of the equations of motion are

$$w_\tau = \nabla_\gamma^2 w + 1/\gamma\,[\psi, w] + 1, \tag{7}$$

$$\theta_\tau = 1/Pr\,\nabla_\gamma^2\theta + 1/\gamma\,[\psi, \theta] + w, \tag{8}$$

$$\Omega_\tau = \nabla_\gamma^2\Omega + 1/\gamma\,[\psi, \Omega] - \lambda(1/\gamma\,\theta_x \cos\phi - \theta_y \sin\phi), \tag{9}$$

$$\nabla_\gamma^2\phi + \Omega = 0, \tag{10}$$

where

$$\nabla_\gamma^2 = 1/\gamma^2\,\partial_{xx} + \partial_{yy}, \quad [f, g] := f_x g_y - f_y g_x, \quad \lambda = \frac{g\beta a^7}{\rho\nu^4}\left(\frac{dp'}{dz'}\right)\left(\frac{dT_b'}{dz'}\right), \quad Pr = \frac{C_p\mu}{k}.$$

The scales used here differ slightly from the ones used in (I). The lengthscales are chosen such that the aspect ratio γ appears explicitly in the equations. The computational domains are independent of γ and are given by $R^+ := \{(x, y)| -1 \leqslant x \leqslant 1, 0 \leqslant y \leqslant 1\}$ and $R := \{(x, y)| -1 \leqslant x \leqslant 1, -1 \leqslant y \leqslant 1\}$, respectively, for the stationary symmetric and non-symmetric cases. This has certain advantages in the path-following schemes with respect to aspect ratio. The axial velocity and temperature scales are chosen such that the mean axial velocity does not explicitly appear in the equations of motion. Hence, the dynamical parameter appearing explicitly in the above equations is λ which is related to the Grashof number (defined in (I) as $Gr = a^3\beta g Q'/k\nu^2$) by $Gr = \lambda A \langle w \rangle Pr$, where $\langle w \rangle$ is the mean axial velocity. It is computed after a solution is obtained for a specified λ.

2.1. *Symmetry and boundary conditions*

The no-slip, impenetrability and uniform temperature conditions on the walls result in

$$u = 0, \quad v = 0, \quad w = 0, \quad \psi = 0, \quad \psi_n = 0, \quad \theta = 0, \tag{11}$$

where, ψ_n denotes the normal derivative at the wall. The boundary condition for the vorticity on the wall is derived from a Taylor series expansion together with the above conditions. Its specific form will be given in §4. For $\phi = 0$ the equations admit solutions with the following symmetry properties:

$$\left.\begin{array}{ll} u(-x, y) = -u(x, y), & v(-x, y) = v(x, y), \\ w(-x, y) = w(x, y), & \theta(-x, y) = \theta(x, y), \\ \Omega(-x, y) = -\Omega(x, y), & \psi(-x, y) = -\psi(x, y). \end{array}\right\} \tag{12}$$

Hence, the boundary conditions on the line of symmetry $(x = 0)$ are

$$w_x = 0, \quad \theta_x = 0, \quad \psi = 0, \quad \Omega = 0. \tag{13}$$

For $\phi \neq 0$ the solution must be obtained over R. The solutions for $\phi < 0$ can be constructed from those for $\phi > 0$ using the following symmetry property:

$$u(-x, y; -\phi) = -u(x, y; \phi), \quad v(-x, y; -\phi) = v(x, y; \phi),$$
$$\left.\begin{array}{l} w(-x, y; -\phi) = w(x, y; \phi), \quad \theta(-x, y; -\phi) = \theta(x, y; \phi) \\ \Omega(-x, y; -\phi) = -\Omega(x, y; \phi), \quad \psi(-x, y; -\phi) = -\psi(x, y; \phi). \end{array}\right\} \quad (14)$$

The friction factor is defined as

$$fRe = 8\gamma^2 / [(1+\gamma)^2 \langle w \rangle], \quad (15)$$

where the average axial velocity is given by

$$\langle w \rangle = \int_{-1}^{1} \int_{-1}^{1} w \, \mathrm{d}x \, \mathrm{d}y / (\text{Area}).$$

The Nusselt number is defined by

$$Nu = \frac{4\gamma^2}{(1+\gamma)^2} \frac{\langle w \rangle Pr}{\langle \theta_b \rangle}, \quad (16)$$

where the average bulk temperature $\langle \theta_b \rangle$ can be computed from

$$\langle \theta_b \rangle = \int_{-1}^{1} \int_{-1}^{1} w\theta \, \mathrm{d}x \, \mathrm{d}y / (\text{Area}) \langle w \rangle.$$

3. Positivity of w and θ and mean-square estimates

We wish to derive some *a priori* bounds for stationary solutions of the boundary-value problem (7–11). Let R be an arbitrary two-dimensional domain such that Green's first identity holds. The variables x, y are scaled such that $\gamma = 1$ in (7)–(10). The following relations hold for any $f, g, h \in C^1(R)$:

$$\int_R h[f, g] \, \mathrm{d}R = -\int_R f[h, g] \, \mathrm{d}R \quad (17)$$

provided $f = 0$ or $h = 0$ on the boundary ∂R of R,

$$\int_R [f, g] \, \mathrm{d}R = 0, \quad \int_R f[g, f] \, \mathrm{d}R = 0 \quad (18)$$

if $f = 0$ or $g = 0$ on ∂R, and

$$\lambda_1 \int_R f^2 \, \mathrm{d}R \leqslant \int_R |\nabla f|^2 \, \mathrm{d}R, \quad f = 0 \quad \text{on} \quad \partial R, \quad (19)$$

where λ_1 is the smallest eigenvalue of $\nabla^2 u + \lambda u = 0$, $u = 0$ on ∂R. To prove (17), set $v = fh(g_y, -g_x)$ and apply the divergence theorem; (18) is proved similarly.

We first show that $w(x, y)$ and $\theta(x, y)$ are positive in R. Multiplying (7) by w and (8) by θ and integrating by parts, one finds, using (11) and (17),

$$\int_R |\nabla w|^2 \, \mathrm{d}R = \int_R w \, \mathrm{d}R > 0, \quad (20)$$

$$\frac{1}{Pr} \int_R |\nabla \theta|^2 \, \mathrm{d}R = \int_R w\theta \, \mathrm{d}R > 0. \quad (21)$$

Pr	$\int \lvert \nabla w \rvert^2 \mathrm{d}R$	$A_R \lambda_1^{-1}$	$\int \lvert \nabla \theta \rvert^2 \, \mathrm{d}R$	$Pr^2 A_R \lambda_1^{-3}$	$\int (\theta + w^2) \, \mathrm{d}R$	$(1 + Pr) A_R / \lambda_1^2$
5.0	0.5075	0.8106	0.2108	0.8321	0.3436	0.9855
3.0	0.4948	0.8106	0.0862	0.2996	0.2576	0.6570
1.0	0.4910	0.8106	0.0132	0.0333	0.1592	0.3285
0.73	0.4976	0.8106	0.0076	0.0177	0.1460	0.2842

TABLE 1. Comparison of mean-square estimates

If $w < 0$, it must assume a local minimum inside R, say at $P_0 = (x_0, y_0)$. Hence $w_x = w_y = 0$ at P_0. Thus $\nabla^2 w = -1$ from (7), which is not possible at a relative minimum. The same argument shows that $\theta(x, y) > 0$ in R, since at P_0 where $\nabla \theta = 0$, (8) yields $\nabla^2 \theta = -Prw(x_0, y_0) < 0$.

Next, we apply the Schwarz inequality to the right-hand side of (20), followed by an application of (19),

$$\int_R \lvert \nabla w \rvert^2 \, \mathrm{d}R \leqslant A_R^{\frac{1}{2}} \left(\int_R w^2 \, \mathrm{d}R \right)^{\frac{1}{2}} \leqslant \left(\frac{A_R}{\lambda_1} \right)^{\frac{1}{2}} \left(\int_R \lvert \nabla w \rvert^2 \, \mathrm{d}R \right)^{\frac{1}{2}},$$

where A_R is the area of R. It follows that

$$\int_R \lvert \nabla w \rvert^2 \, \mathrm{d}R \leqslant A_R \lambda_1^{-1}. \tag{22}$$

The same procedure applied to the right-hand side of (21) yields, in view of (22),

$$\int_R \lvert \nabla \theta \rvert^2 \, \mathrm{d}R \leqslant (Pr)^2 A_R \lambda_1^{-3}. \tag{23}$$

Finally, multiplying (7) by θ and (8) by w and following the same steps, again using (17), one finds

$$\int_R (\theta + w^2) \, \mathrm{d}R \leqslant (1 + Pr) A_R \lambda_1^{-2}. \tag{24}$$

Note that these bounds are independent of λ. Along these lines similar estimates can be derived for Ω and $\nabla \psi$. These results are

$$\int_R \Omega^2 \, \mathrm{d}R \leqslant \lambda^2 Pr^2 A_R \lambda_1^{-5}, \quad \int_R \lvert \nabla \psi \rvert^2 \, \mathrm{d}R \leqslant \lambda^2 Pr^2 A_R \lambda_1^{-6}. \tag{25}$$

The *a priori* bounds for Ω and $\nabla \psi$ depend also on λ.

The above bounds, valid for any solution of the stationary boundary-value problem (7)–(11), turn out to be surprisingly close to the actual numerical solutions. Table 1 shows a comparison of numerically computed left-hand sides of (22)–(24) at $\lambda = 2.40723$ with the rigorously derived bounds for a square with zero tilt. One may hope to use these bounds for proving uniqueness of stationary solutions for sufficiently small λ and in providing estimates of uniqueness ranges in the parameter space. We shall, however, not pursue this matter further here. In the limit case $\lambda = 0$ the equations (7)–(11) become linear. Moreover, from the structure of (7)–(11) we expect the number of regular solutions to remain odd with increasing λ.

4. Numerical methods

4.1. *Numerical algorithms*

We are interested primarily in the stationary solutions to (7)–(10). Transient simulations are presented in Fung, Nandakumar & Masliyah (1987). But they are useful only as a means of reaching a steady state. Transient, two-dimensional solutions are not physically realizable in an experiment as they are inconsistent with the axial invariance or fully developed flow assumption. In other words we expect any disturbance at an axial position to grow (or decay) with time as well as be carried downstream by the forced axial flow. In regions of the parameter space where there are multiple solutions, the pseudo-transient simulation may converge to any one of the stationary solutions, depending on the initial starting condition, the stability and the region of attraction of the stationary solution. A different set of algorithms are better suited to uncover the stationary solution structure without regard to the above factors. We here employ the Newton method, which has become a standard tool for solving nonlinear boundary value problems. Hence, only a brief outline is given here, followed by an outline of the discretization scheme. Whenever we refer to (7)–(10) in this section, we mean the stationary form of (7)–(10). Together with the boundary conditions (11) they can be written symbolically as a single equation,

$$f(u, p) = 0, \tag{26}$$

where $u := (w(x, y), \theta(x, y), \Omega(x, y), \psi(x, y))$ and $p = \{\lambda, Pr, \gamma, \phi\}$ is the parameter set. The Newton method amounts to finding the successive corrections $U_n = (W_n, T_n, O_n, P_n)$ at each step of the iteration from the linearized form of (26) which is $f_u(u_n, p) U_n = r_n$. Dropping the subscript n, the explicit form of the linearized equation is

$$\Delta_\gamma W + 1/\gamma \left([\psi, W] + [P, w]\right) = r_1, \tag{27}$$

$$\frac{1}{Pr} \Delta_\gamma T + 1/\gamma \left([\psi, T] + [P, \theta]\right) + W = r_2, \tag{28}$$

$$\Delta_\gamma O + 1/\gamma \left([\psi, O] + [P, \Omega]\right) - \lambda(1/\gamma \, T_x \cos \phi - T_y \sin \phi) = r_3, \tag{29}$$

$$\Delta_\gamma P + O = r_4, \tag{30}$$

and the boundary conditions are

$$W = T = P = \partial P/\partial n = 0, \tag{31}$$

r_1, r_2, r_3, r_4 being the residuals. To start the calculation on any solution branch, a converged solution at one set of parameter values is needed. This is most easily generated for $\lambda = 0$ as the nonlinear terms in (7)–(10) drop out and the Newton scheme converges in one iteration to machine precision. Euler–Newton continuation is then used to obtain solutions at other values of the parameters. The parameter can be any one from the set p, although we have primarily used continuation with respect to λ. This entails computing the tangent vector to the solution path at the current value of λ, $\dot{u} = \partial u/\partial \lambda$. This is obtained from $f_u(u, p) \dot{u} = -f_\lambda$ which requires only one additional solution of (27)–(31) with r_n replaced by $f_\lambda = (0, 0, ((1/\gamma) \theta_x \cos \phi - \theta_y \sin \phi), 0)$. Similar derivatives with respect to other parameters can be obtained from (7)–(10). When such a continuation fails at some value of λ, it usually indicates the presence of singular point in the vicinity of λ. At this stage the problem is reparametrized in terms of a pseudoarclength parameter, s, as proposed by Keller (1977). The parameter λ is treated as an element of the unknown vector $(w(s), \theta(s), \Omega(s), \psi(s), \lambda(s))$ which provides a degree of freedom to extend the basic equations

(7)–(10) by an equation defining the arclength and thus making the extended system regular. We take this constraint to be

$$w_1 \iint \{\dot{w}(w(s) - w(s_0)) + \dot{\theta}(\theta(s) - \theta(s_0)) + \dot{\Omega}(\Omega(s) - \Omega(s_0))$$

$$+ \dot{\psi}(\psi(s) - \psi(s_0))\} \, dx \, dy + w_2 \dot{\lambda}(\lambda(s) - \lambda(s_0)) = (s - s_0), \quad (32)$$

with positive weights w_i, $i = 1, 2$. The resulting extended system of equations (7)–(10) and (32) is also solved by the Newton method for a specified s and this procedure has no difficulty in turning around limit points. A simple step-length adjustment procedure, which adjusts Δs such that the Newton iteration converges to specified tolerance within three iterations, was found to be adequate to turn around even sharp corners.

Simple quadratic limit points on a solution path $u = u(\lambda)$ are determined from the following extended system of equations proposed by Moore & Spence (1980) and Spence & Werner (1982):

$$f(u, \lambda) = 0, \quad f_u(u, \lambda) \, v = 0, \quad m(v) = 1. \quad (33)$$

In (33) v is the right null vector, and the constraint $m(v) = 1$ enforces the null vector to be non-trivial. This system is known to be regular and can be solved by the Newton scheme for the unknowns $\chi := (u, v, \lambda)$. Note that if we let $v = (\tilde{w}, \tilde{\theta}, \tilde{\Omega}, \tilde{\psi})$, then the additional set of equations for v, symbolically represented in (33) as $f_u(u, \lambda) v = 0$, are precisely (27)–(31) with the operand U replaced by v and the right-hand side replaced by 0. These are of course nonlinear in the variable set χ. Writing (33) as a formal operator equation $\Phi(\chi, p) = 0$, the Newton equations are obtained by taking the Fréchet derivative of $\Phi(\chi, p)$ with respect to χ. The discretized version of (33) has a block structure with the operator f_u appearing twice and hence the resulting equations can be most efficiently solved using the triple bordered scheme, the details of which can be found in Weinitschke (1985). While the initial guess for u is available from continuation on the solution path, that for v is estimated by a limit-point monitoring scheme devised by Weinitschke (1985).

The symmetry S defined by (12) may be written symbolically as $f(Su, p) = Sf(u, p)$, with f defined in (26). Symmetry-breaking bifurcation points, which lie on the path of symmetric solutions and spawn asymmetric solution branches, are determined by a method proposed by Werner & Spence (1984) which uses the same extended system of equations (33), with the restriction $u \in X_s$, $v \in X_a$ where $X_s = \{u \mid Su = u\}$ and $X_a = \{u \mid Su = -u\}$ are the symmetric and antisymmetric subspaces, respectively.

The above algorithms are useful in determining the solution structure as λ is varied, keeping other parameters fixed. In order to determine how this structure unfolds as another parameter (say the aspect ratio, γ) is varied, we need to determine the locus of singular points $(u(\gamma), \lambda(\gamma))$ over a range of γ. Such a locus is often called a *fold curve*. It requires the solution of the extended system (33) for a sequence of γ values, which is best obtained by the Euler–Newton continuation in γ. At some critical point $\gamma = \gamma^*$ the extended system (33) or the system (33) with $u \in X_s$, $v \in X_a$ may itself become singular indicating the presence of higher-order singularities. In such instances the system (33) can be doubly extended (Yang & Keller 1986b) or an arclength continuation can be used in γ. In the present work we have just used the simple continuation with resect to ϕ and γ. Since the higher-order singularities are few in number, they were simply bracketed by interval halving.

In bifurcation theory, the various types of singular points are characterized analytically by certain scalar quantities (e.g. see Jepson & Spence 1985). These 'test quantities' may be evaluated numerically to provide an additional check on the type of singularity computed by the methods described above, that is, they may serve as monitors to discover singular points on a regular solution branch or on a fold curve. For example, let z be the left null vector corresponding to v in (33), then at a limit point $(z, f_\lambda) \neq 0$ while at a bifurcation point $(z, f_\lambda) = 0$ (in a Hilbert space setting $(\cdot, \cdot)$ refers to an inner product). Defining $a_f = (z, f_{uu} vv)$, then $a_f = 0$ signifies a pitchfork, while $a_f \neq 0$ signifies a transcritical bifurcation point. Additional conditions must be satisfied for a complete characterization of these (simple) singular points. In the present problem, it is quite simple to compute a_f.

4.2. *Discretization*

The governing equations (7)–(10) are discretized in the interior of R or R^+ by central difference approximation over a uniform grid. The grid points are numbered as $\{(x_i, y_j) \mid i = 0 \dots N+1, j = 0 \dots M+1\}$. The boundary conditions $w = 0$ (no-slip), $\psi = 0$ (impenetrability) and $\theta = 0$ on the wall are of the Dirichlet type. Axial vorticity, Ω, is however not known on the solid boundaries. One approach to overcome this difficulty has been to combine (9) and (10) and eliminate Ω. This introduces a biharmonic operator for ψ in the combined equation and the normal derivative, $\psi_n = 0$ (no-slip) provides the additional condition for ψ. Such derivative boundary conditions are also discretized by second-order-accurate difference approximations. The discretized form of the biharmonic operator couples 13 unknown nodal values requiring special attention near the boundaries. Also the condition number of the resultant matrix is very large (Allen, Herrera & Pinder 1988). Hence, we follow the alternative approach in which (7)–(10) are retained in their original form and a second-order-accurate vorticity boundary condition is derived through a Taylor series expansion. Such an approach has been used widely (Roache 1972). As an example, the vorticity boundary condition on the left wall $x = -1.0$ is given by

$$\Omega_{0,j} = (8\psi_{1,j} - \psi_{2,j})/[2(\Delta x)^2], \quad j = 1 \dots M,$$

where $(j = 1 \dots M)$ are the nodal points on the wall. The corresponding Newton equations for the corrections, $O_{0,j}$ are

$$O_{0,j} = (8P_{1,j} - P_{2,j})/[2(\Delta x)^2], \quad j = 1 \dots M.$$

Similar conditions apply on the other walls. While seeking symmetric solutions, the discretized five-point formulae used in the interior are also used on the boundary $\{(0, y_j) \mid j = 0 \dots M+1\}$. This introduces a set of points outside the domain of interest which are eliminated by imposing the symmetry conditions,

$$W_{-1,j} = W_{1,j}, \quad T_{-1,j} = T_{1,j} \quad P_{-1,j} = -P_{1,j}, \quad O_{-1,j} = -O_{1,j}. \tag{34}$$

Since the structure of the discretized, linearized equations is sparse, the sparse matrix solver, SPARSPAK (Chu *et al.* 1984) was used to solve equations (27)–(31) and the corresponding linearized form of the extended systems.

5. Results and discussion

The physical mechanisms responsible for the existence of multiple solutions in the Taylor and Rayleigh–Bénard problems are well understood. Both are closed systems with no net flow through the observational domain. In the former case a centrifugally

unstable flow field exists when the inner cylinder rotates faster than the outer one. In the latter case an unstably stratified density field in a gravitational environment exists when the bottom wall is heated. In both cases viscosity acts as a damping mechanism and the primary flow at very low values of the dynamical parameter (viscous dominated) is both unique and stable. As the external forcing is increased, additional solutions bifurcate from the primary solution at certain critical values of the dynamical parameter.

The Dean problem is a variant of the Taylor problem. In an identical sense, the Morton problem can be considered a variant of the Rayleigh–Bénard problem. Both the Dean and Morton problems are open systems since the flow is driven by an imposed pressure gradient through the observational domain. In the Dean problem with zero velocity condition around a duct wall, a centrifugally unstable flow regime exists only near the outer region of the curved duct where the streamwise velocity component decreases with increasing radius. Similarly, in the Morton problem with uniform temperature around the periphery, an unstably stratified density field exists only near the bottom wall when the fluid is heated uniformly. Once again viscosity acts as a damping mechanism and at low values of Dn or Gr, the primary flow is unique and stable. However, it consists of a primary flow driven by the applied pressure gradient and a secondary flow with two counter-rotating vortices driven respectively by the centrifugal and buoyancy forces. When the strength of the centrifugal or buoyancy force is increased relative to that of the viscous force, additional solutions bifurcate at certain critical points. Thus the physical mechanisms responsible for the primary solution becoming unstable and additional solutions bifurcating from them are well understood for these classes of problems.

The questions concerning the solution structures, flow structures and their experimental realizability have been resolved to a far greater extent on the Dean problem than in the Morton problem. Appropriate comparisons are made between the mixed-convection problem and the Dean problem throughout this section. By solution structure we mean the number of solution branches and their connectivity through different types of singular points. By flow structure we mean the secondary flow patterns at any given set of parameter values. Recognizing that at a point in the parameter space, several different solutions with quite different flow structure can coexist, a uniform grid that is fine enough to resolve all the different flow structures is used. The pair of numbers $(N \times M)$ represent the number of grid points used in the x- and y-directions, respectively. Some grid sensitivity results are presented in table 2 for $\gamma = 1.0$, $Pr = 0.73$, $\phi = 0°$, using grids of (9×19), (14×29) and (19×39). The asymmetric solutions are of course obtained over the full domain. Since they occur in pairs, with one being the mirror image of the other, the macroscopic results in table 2 are presented for only one of the pair. In the forced-convection limit of $\lambda = 0$ the literature (Shah & London 1978) values of fRe and Nu are reproduced to within 1 %. At $\lambda = 3 \times 10^6$ there are five different solutions, three of which are symmetric. The various solutions for this case are identified using the labels introduced in figure 2(*d*). The macroscopic results on a grid (14×29) are found to be in agreement with the results on the finer grid (19×39) to within 1 %. There is also no qualitative change in the solution structure as the grid is refined from (9×19) to (19×39) over the range of λ which is of interest. The detailed parametric study of the solution structure has been carried out using a grid of (14×29).

An additional check on the accuracy of our solutions was performed by solving the basic equations (1)–(5) in terms of the primitive variables (u, v, w, p, T). We used a general PDE-program (written by Dobrowolski) based on a finite-element multigrid

(a) Solution		9×19	14×29	19×39	
Forced conv.	fRe	14.2584	14.2410	14.2349	
$\lambda = 0$	Nu	3.5994	3.6042	3.6058	
unique 2-cell	fRe	19.6916	19.6134	19.5931	
$\lambda = 25$	Nu	5.9127	5.9203	5.9261	
1 on IS1	fRe	26.1558	25.8017	25.7173	
$\lambda = 3 \times 10^6$	Nu	8.6015	8.5550	8.5586	
2 on IS1	fRe	27.1097	26.7127	26.6082	
$\lambda = 3 \times 10^6$	Nu	8.7507	8.6924	8.6907	
3 on PM	fRe	28.2905	27.8406	27.7118	
$\lambda = 3 \times 10^6$	Nu	9.4243	9.3324	9.3171	
4 on AS2	fRe	26.2448	25.8124	25.7112	
$\lambda = 3 \times 10^6$	Nu	8.5595	8.5032	8.5047	

(b) Singular point		9×19	14×29	19×39	24×49
L1	λ	517384	516737	516828	516882
	Gr	139225.64	139811.46	140011.21	140082
	fRe	21.7023	21.5844	21.5574	21.5487
	Nu	6.6532	6.6547	6.6622	6.6673
L2	λ	769238	821757	842538	852366
	Gr	202837.78	216570.95	221805.98	224232 96
	fRe	22.1475	22.1593	22.1834	22.4233
	Nu	6.9339	7.0026	7.0367	7.0546
SB1	λ	740543	798048	820348	830850
	Gr	195887.96	210866.02	216482.98	219079.85
	fRe	22.0778	22.1022	22.1303	22.1479
	Nu	6.8922	6.9691	7.0057	7.0247

TABLE 2. Grid sensitivity tests: (a) fRe and Nu at regular points; (b) singular points, λ, Gr ($\gamma = 1.0$, $Pr = 0.73$, $\phi = 0°$)

method. To demonstrate how accurately our finite-difference solutions are reproduced by this method, we first checked the case $\lambda = 0$ and obtained the following data for various values of the maximal step size H: for $H = \frac{1}{16}$, $fRe = 14.4092$ and $Nu = 3.6529$, for $H = \frac{1}{32}$ these two values are 14.2755 and 3.6174, and for $H = \frac{1}{64}$ they are 14.2349 and 3.6125, respectively. These values almost coincide with those of table 2(a) for $\lambda = 0$. Similarly, the accuracy of our results for $\lambda \neq 0$ has been verified by the finite-element-method multigrid program at selected points on the primary branch.

Table 2(b) shows data on numerical convergence at singular points. Note that the limit point L1 is isolated, but the limit point L2 (almost) coincides with the symmetry-breaking bifurcation point SB1. The values of λ and Gr as well as the fRe and Nu values are shown for each of the three singular points for various grid sizes. It is seen that the convergence for the limit point L1 with increased grid refinement is at least as good as for the regular points (table 2a), while for the close pair of singular points L2/SB1 convergence is significantly slower than at regular points. The limit point L2 was bracketed in (I) to lie around $Gr = 225000$. The most accurate estimate of L2 obtained in the present work using a (24×49) grid is $Gr = 224233$. We did not find spurious singular points on very coarse grids which disappear on grid refinement, as was observed by Winters (1987).

The solution structure and flow structure are well resolved on all the three grids

used here over the range of λ of interest. These ranges are for $Pr = 0.73$, $0 \leqslant \lambda \leqslant 7 \times 10^6$ and for $Pr = 5.0$, $0 \leqslant \lambda \leqslant 10^5$. After a suitable scaling of variables ($\bar{\theta} = 100\theta$, $\bar{\Omega} = \Omega/100$, $\bar{\lambda} = \lambda/10^4$) the continuation method had no difficulty in taking large steps (of the order of $\bar{\lambda} \sim 10$) except near turning points, and in converging in three Newton iterations for λ values much larger than the limits used here. Several additional limit points were also found at higher values of λ. These, however, have not been studied in greater detail for the following reasons. Even at $\lambda \sim 3 \times 10^6$ and $Pr = 0.73$ all the known two-dimensional solutions develop some form of unstable modes. Hence from the point of experimental realizability such solutions at higher λ values are of less importance. Also, the development of sharp boundary layers on the sidewalls at higher λ values necessitate the use of finer and/or non-uniform grids. Questions such as whether there are infinitely many solutions with increasing number of vortices as $\lambda \to \infty$ (as conjectured for example by Yang & Keller 1986a on the Dean problem) and whether these solutions are connected to the experimentally realizable solutions at lower values of λ and higher aspect ratios are clearly of interest. But they have not been addressed in the present work.

5.1. *Solution structure for a square duct*

The solution structure for $\gamma = 1$, $\phi = 0°$, $Pr = 0.73$ is illustrated in figure 2(*a–d*). In these, four different projections of the solution paths are shown. Since these are only one-dimensional projections of the solution paths, some paths may appear to intersect in certain projections and other branches that are distinct may appear to be coincident. To be a true bifurcation point, however, they must intersect at the same value of Gr in every possible projection – i.e. the entire solution vector of the discretized problem should be the same at such critical points. Figures 2(*a*) and 2(*b*) show respectively, the Nusselt number and fRe variation with Gr. Since these are integrated quantities, the differences in their values corresponding to different solution branches at the same Gr are not always significant enough to be seen graphically. Also, the two parts of the asymmetric branches are overlaid. The stars in figure 2(*a*) show recent results of Van Dyke (1990) obtained for a circular cross-section. It appears that the $\frac{2}{15}$ power law suggested in his work for the Nu vs. Gr relationship corresponds to the asymptotic behaviour of our two-cell branch.

Two other quantities, viz. the stream function and axial velocity at the location $(x, y) = (0.133, 0.133)$ are used as the state functions in figure 2(*c, d*). This spatial location is chosen since the flow profile changes most significantly in this region and both branches of any asymmetric solution are made visible. True singular points are marked in these figures. Simple limit points and the symmetry-breaking bifurcation points are labelled in ascending numerical order as Ln and SBn, respectively, for $\gamma = 1, Pr = 0.73$. The critical values of both λ and Gr and the branches on which they lie are shown in table 3. Branches of fold curves originating from this reference point ($\gamma = 1$, $Pr = 0.73$) are referred to by the same labels even though the relative magnitudes of the singular points can change as γ and Pr are varied.

Various parts of the solution branches were constructed using the following general approach. Starting from $\lambda = 0$ and using arclength continuation, the entire branch PM was generated easily by solving over R^+. The lower and upper parts of the branch PM in figure 2(*a, b*) correspond, respectively, to the two- and four-cell flow structures computed in (I). Considering that the limit points in (I) were only bracketed approximately, the agreement is quite good. Based on experience with similar problems (Weinitschke, Nandakumar & Ravi Sankar 1990) we expect to find a symmetry-breaking point very close to L2 and an asymmetric branch to originate
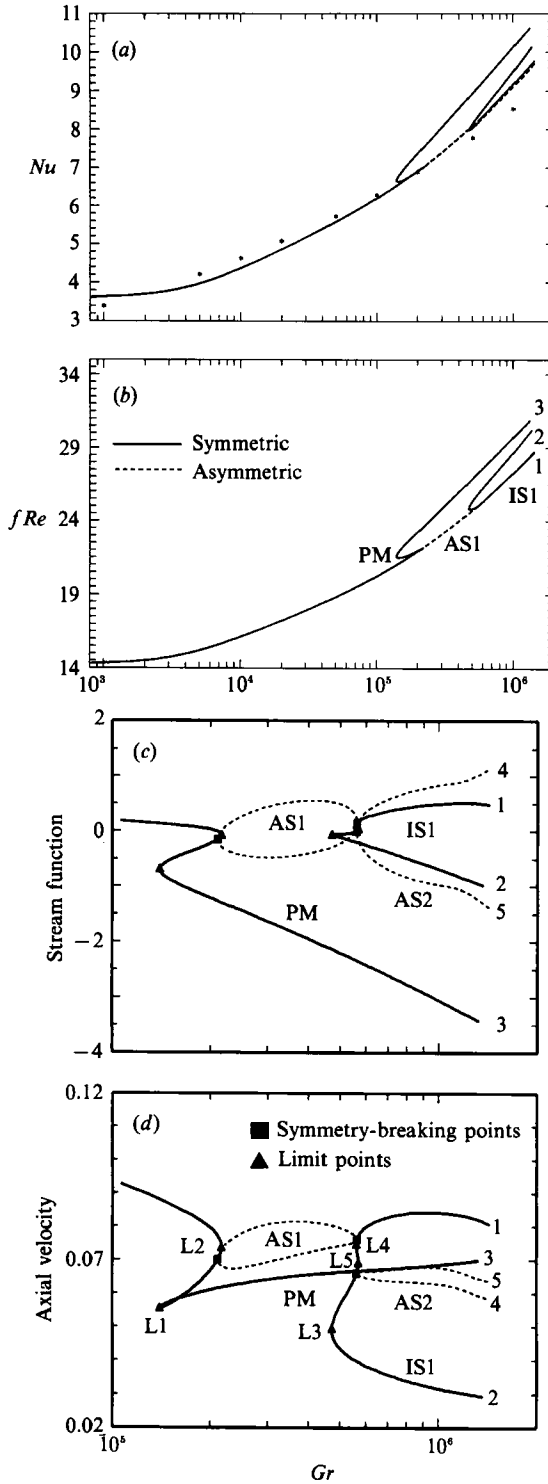
FIGURE 2. State diagram showing the solution structure for $\gamma = 1.0$, $\phi = 0°$, $Pr = 0.73$. (a) Nu vs. Gr, (b) fRe vs. Gr, (c) stream function at node $(2,2)$ vs. Gr, and (d) axial velocity at node $(2,2)$ vs. Gr. L1 to L5 refer to limit points; PM to a primary branch; IS1 to an isolated symmetric branch; AS1, AS2 to asymmetric branches. In (c, d) both the branches of asymmetric solutions are visible.

from there. A regular solution on the asymmetric branch was readily generated by starting with a solution just below L2, tilting the duct by 1°, increasing λ past L2 and finally bringing the tilt back to 0°. The branch AS1 is then completed by using the arclength scheme, applied over the full domain. The branch turns around and forms a closed loop. The presence of additional singular points was checked in the region of the turning point at the far end of the asymmetric branch AS1. In this way, the almost coinciding singular points L4 and SB2 were found. This suggests that an isolated symmetric branch separated from PM must exist. A regular solution on this branch, IS1, was easily generated by starting with a solution just below SB2 as an initial guess and solving over R^+ at a λ value just above SB2. Then continuing with the arclength scheme on either direction, the entire branch IS1 that lies within $\lambda \leqslant 7 \times 10^6$ was computed. During the course of this computation the arclength continuation scheme turned around three additional limit points, L3, L4 and L5, the precise locations of which were computed using the extended system.

Note that each pair of singular points (L2,SB1) and (L4,SB2) are close. Whether each pair represents just a single point of higher nullity in the continuous problem and whether their slight separation is an artifact of the numerical discretization cannot be ascertained at present. The reflective symmetry that is present at zero degrees is, however, destroyed with even a slight degree of tilt. The solution branches near symmetry-breaking points unfold into smooth process with such a perturbation. To accommodate this possibility, we expected to find another SB point near L5 and an asymmetric branch to originate from there. Using the steps outlined earlier the singular point SB3 and the branch AS2 were located. The limit points L1 and L3 are the only isolated ones, i.e. without a nearby SB point. The others are found to occur very close to SB points which in turn unfold into smooth processes upon tilting the channel, as will be described in detail in §5.5. A total of five different solutions were found at $\lambda = 7 \times 10^6$, and the terminal parts of these branches are labelled 1–5 in figure 2(c, d).

The flow profiles of the five different solutions at $\lambda = 3 \times 10^6$ and $Pr = 0.73$ are shown in figure 3. Figures 3(a)–3(c) show, respectively, the streamline contours, axial velocity perspective plots and the isotherms of a four-cell flow pattern on the branch PM. This corresponds to the four-cell flow already computed in (I). Figure 3(d–f) show similar profiles on the branch IS1 originating at point 2. This is a new four-cell pattern. It is conjectured that upon increasing the aspect ratio to a suitably large value, the first four-cell flow structure (figure 3a–c) will become a genuine primary flow with four cells spanning the entire channel height while the second four-cell structure (figure 3d–f) might be connected to a six-cell primary flow at a suitably large aspect ratio. Such transitions are expected to take place through a series of transcritical bifurcations which was proposed as a mechanism for the primary mode exchange process in the Taylor problem by Benjamin (1978). Figure 3(g–i) shows a two-cell flow structure on the branch IS1 originating at point 1. Figure 3(j–l) shows a two-cell asymmetric flow structure on the branch AS2 originating at point 4. Note that the streamline contours and the axial velocity profile near the bottom wall change quite significantly and hence their choice at spatial position (0.133, 0.133) as the state function in figure 2(c, d) is seen to be a sensitive indicator of changes in flow pattern on various parts of the solution branches.

All the different flow structures shown above have also been computed for the Dean problem (Winters 1987). Since the solution structure is also essentially similar, only the differences are discussed here. While in the Dean problem the isolated symmetric branch has only one limit point we find three limit points in the present

Singular points	Branch	λ	Gr
		$Pr = 0.73$	
L1	PM	0.51673765 10^6	0.13981146 10^6
SB1	PM & AS1	0.79804825 10^6	0.21086602 10^6
L2	PM	0.82175700 10^6	0.21657095 10^6
L3	IS1	0.20073713 10^7	0.47154621 10^6
L4	IS1	0.24174261 10^7	0.56249075 10^6
SB2	IS1 & AS1	0.24198946 10^7	0.56283017 10^6
SB3	IS1 & AS2	0.24279813 10^7	0.56456925 10^6
L5	IS1	0.24517398 10^7	0.56956376 10^6
		$Pr = 5.00$	
L1	PM	0.12433354 10^5	0.32788399 10^5
SB1	PM & AS1	0.23748938 10^5	0.60819487 10^5
L2	PM	0.24072729 10^5	0.61586648 10^5
L3	IS1	0.39933373 10^5	0.10102388 10^6
L4	IS1	0.53264439 10^5	0.13163878 10^6
SB2	IS1 & AS1	0.54241702 10^5	0.13440622 10^6
SB3	IS1 & AS2	0.53482152 10^5	0.13200779 10^6
L5	IS1	0.54880903 10^5	0.13576532 10^6

TABLE 3. Singular points at $\gamma = 1.0$, $\phi = 0°$ (14×29H or 29×29F). Ln is a limit point on a symmetric branch, SBn a symmetry-breaking point

problem. The asymmetric branch AS1 originates from near L1 in both problems. It is, however, connected to IS1 in the present problem while it remains disconnected, at least within the range of parameter q covered by Winters. Additional limit points are found on AS1 in the Dean problem while none is found in the present case. Since arclength schemes can jump branches, particularly in a region where several branches are present, we have taken extra precautions to resolve the connectives between (L4/SB3) and (L5/SB2). Using small arclength steps we do find that the branches AS1 and AS2 turn around at SB3 and SB2 respectively. The branch connecting L4 and L5 is found to be symmetric. The present structure is also appealing from the following viewpoint. As will be shown later, the two-cell part of the branch IS1 originating at point 1 becomes connected to the two-cell part of the primary branch originating at the origin ($\lambda = 0$) upon tilting the duct even slightly. Hence it appears that the AS1 branch must link the branches PM and IS1 to provide for such an unfolding upon tilt.

5.2. *Stability of solutions*

The solution at $\lambda = 0$ is both unique and stable. Changes in the linear stability of the solution along the branches could be monitored by monitoring the sign changes in the determinant of the Jacobian as was done by Winters (1987). An alternative approach is to recognize that the complex function $\beta = (1+z)/(1-z)$ maps the left half-plane onto the interior of the unit circle; hence the eigenvalues of the matrix $\boldsymbol{B} = -(\boldsymbol{A}-\boldsymbol{I})^{-1}(\boldsymbol{A}+\boldsymbol{I})$ are all inside the unit circle, if all the eigenvalues, σ_i of $\boldsymbol{A}$ have negative real parts. Hence computing only the largest eigenvalue of $\boldsymbol{B}$ by the simple (and inexpensive) power iteration determines the stability.† Certain limitations in

† We thank Professor Dobrowolski, Institut für Angewandte Mathematik, Universität Erlangen – Nürnberg, for suggesting this approach.
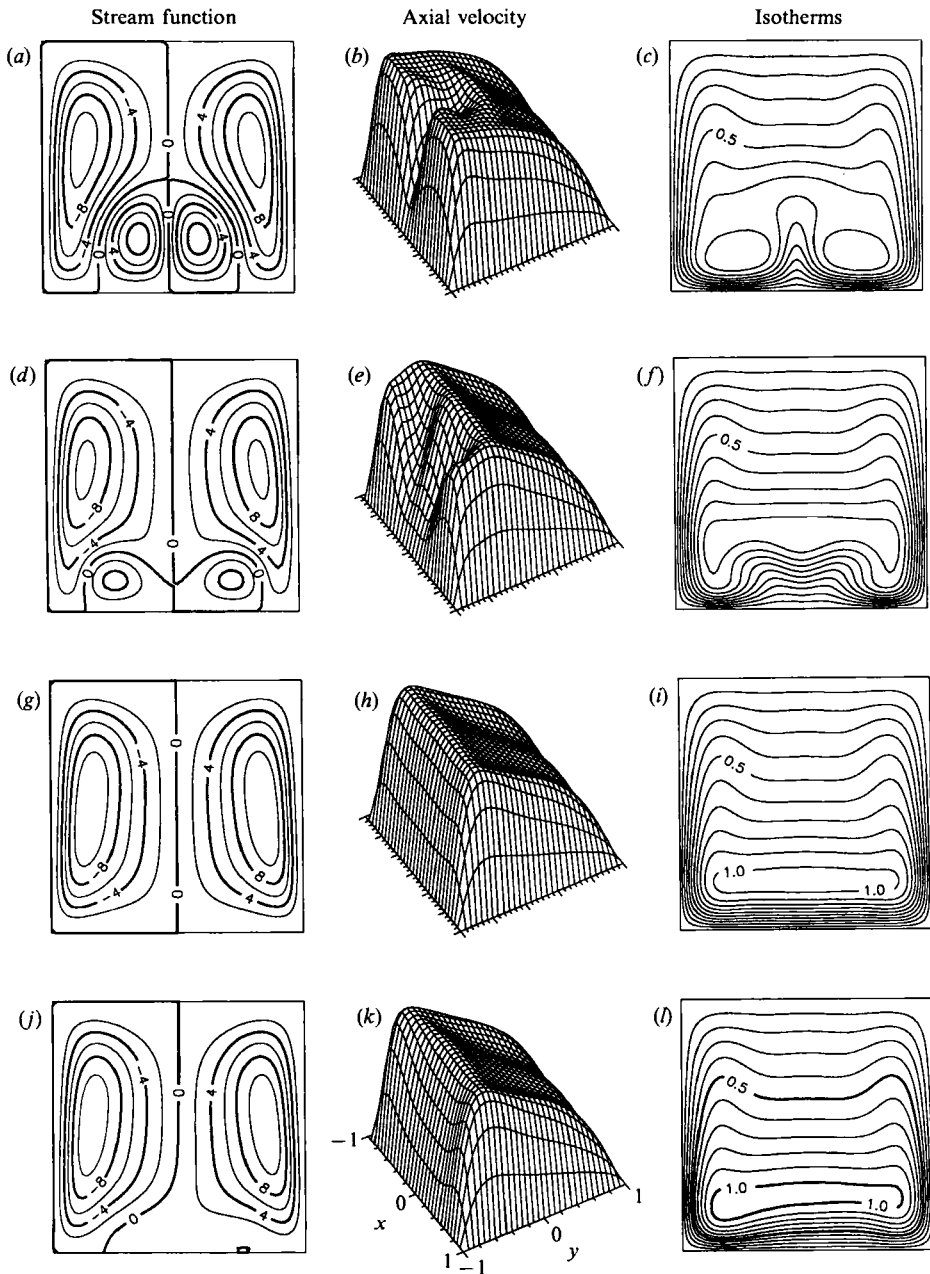
Stream function   Axial velocity   Isotherms

FIGURE 3. Five solutions are present at $\lambda = 3 \times 10^6$ and $Pr = 0.73$, $\gamma = 1.0$, $\phi = 0°$. These are labelled as points 1–5 in figure 2 (c, d). (a) Streamline contours, (b) axial velocity perspective plots and (c) isotherm contours are shown for a four-cell pattern which lies on the branch PM (point 3). $(d–f)$ Similar profiles for another four-cell pattern on the branch IS1 (point 2). $(g–i)$ A two-cell pattern on the branch IS1 (point 1). $(j–l)$ An asymmetric solution on the branch AS2 (point 4). Note that its mirror image (not shown) corresponds to point 5.

Branch	λ	Flow pattern	R^+ or R	Eigenvalues of Jacobian $\boldsymbol{A}$ with positive real parts $M = 19$	Power iteration on $\boldsymbol{B}$ $M = 39$
PM	6×10^5	2-cell	Half	Stable	Stable
			Full	$0.0307 \pm i0.1776$ (spurious)	Stable
PM	6×10^5	weak	Half	0.0532	Unstable
		4-cell	Full	0.0463	Unstable
PM	6×10^5	strong	Half	Stable	Stable
		4-cell	Full	0.0862	Unstable
PM	3×10^6	4-cell	Half	$(0.0615 \pm i0.235)$	Unstable
		(point 3)	Full	$(0.1746, 0.0337 \pm i0.223)$	Unstable
IS1	3×10^6	2-cell	Half	$0.0316 \pm i0.415$	Unstable
		(point 1)	Full	$0.0546 \pm i0.253$	Unstable
IS1	3×10^6	4-cell	Half	$(0.398, 0.0613 \pm i0.4314)$	Unstable
		(point 2)	Full	$(0.249, 0.157, 0.070 \pm i0.262)$	Unstable
AS2	3×10^6	Asymmetric	Full	5 complex pairs	Unstable

TABLE 4. Summary of eigenvalue calculations ($\gamma = 1.0$, $\phi = 0°$, $Pr = 0.73$)

this method must be recognized. Any two-dimensional, time-dependent solution branch that emerges at a Hopf point cannot be detected by monitoring the sign of the determinant alone. Although such solutions are physically unrealizable, their presence has important consequences for the stability picture. The convergence of the power iteration method is often slow, since the mapping brings the eigenvalues close to each other. Also, stability of these solutions with respect to three-dimensional perturbations cannot be determined within the present formulation. Computation of the complete eigenvalue spectrum along the solution branches is a computationally very expensive process. Hence we have used a combination of the power iteration and eigenvalue spectrum computation at selected points on the branches to piece together the following stability picture. It is admittedly incomplete, as the presence of any bifurcating three-dimensional stationary solutions as well as two-dimensional time-dependent solutions have not been taken into account. The entire eigenvalue spectrum was computed only on a coarse grid of (19×9) over R^+ and (19×19) over R. Power iteration was used on finer grids of up to (39×19) over R^+ to check if the largest eigenvalue of $\boldsymbol{B}$ lies within the unit circle. For $Pr = 0.73$ a single pair of complex eigenvalues appeared at $\lambda = 6.0 \times 10^5$ on the two-cell part of the primary branch PM when a coarse grid was used over full domain. We expect this branch to remain stable up to the limit point L2. Hence this pair of complex eigenvalues will be spurious; in fact, it disappeared upon grid refinement. The computed eigenvalues are summarized in table 4. The results from power iteration are indicated either as stable or unstable depending on whether the largest value lies within the unit circle or not. For $\lambda = 6 \times 10^6$, the power iteration on the finest grid always converged to a complex pair which was detected using the algorithm outlined in Holger (1988).

We shall now examine the stability of the three solutions on the primary branch, PM at $\lambda = 6 \times 10^5$. The two-cell solution remained stable. Passing through the pair of points (L2,SB1) to the middle part of PM, two positive eigenvalues were found, one corresponding to symmetric mode (eigenfunction) and the other corresponding to the asymmetric one. Turning around L1, the eigenvalue corresponding to the symmetric mode becomes negative, leaving one positive eigenvalue corresponding to an unstable asymmetric one. This was the only unstable mode found at $\lambda = 3 \times 10^6$

also. Thus the symmetric four-cell solutions on the branch PM are unstable with respect to asymmetric perturbations. This implies that any pseudo-transient simulation that imposes symmetry boundary conditions would find the four-cell solution to be stable. This behaviour is quite analogous to that found in the Dean problem (Winters 1987).

Some comments on the observability of the four-cell flow structure in mixed convection experiments are in order. In the Dean problem such flows have been observed, contrary to their predicted instability. In three-dimensional simulations of Dean flow also we have found the spontaneous development of such four-cell flows (Ravi Sankar *et al.* 1988) from a parabolic inlet profile and their persistence in an axially invariant state over significant length of the duct even while solving over the full domain. This suggests that the growth rates of these asymmetric, unstable modes must be so small that they do not destroy the symmetric, four-cell flows rapidly. However, when the flow is perturbed strongly in an asymmetric fashion, the four-cell flow was never recovered. Instead streamwise periodic mode was triggered. We have carried out similar three-dimensional computations (Ravi Sankar *et al.* 1991) on the mixed-convection problem and have observed similar behaviour. Near the limit point L1 on the four-cell part of the branch the positive eigenvalue is 0.0862 while the eigenvalue with the largest magnitude is -10.8. Near singular points, such small growth rates are to be expected. Upon increasing the λ to 3×10^6 on the same branch the magnitude of the positive eigenvalue increased only modestly to 0.1746. Thus the linear growth rates of this unstable mode are quite small and hence such flows are quite likely to be observed as long as sufficient precautions are taken to ensure a clean inlet profile and a perfect duct alignment with respect to the gravitational direction.

Although a number of experimental works exist on the mixed-convection problem (see (I) for the references) most of them are confined to measuring macroscopic quantities like the heat transfer coefficients in circular ducts. Only recently, Cheng & Yeun (1987) have examined the flow structure of secondary flows in isothermally heated horizontal ducts through visualization techniques. Unlike in the uniform flux case, the strength of the secondary flow decreases in an axially isothermal case as the fluid warms up to the wall temperature. Clearly more experimental effort is needed on identifying the flow structure in the mixed-convection problem.

Returning to other solution branches, at $\lambda = 3 \times 10^6$ a full eigenvalue computation on the coarse grid revealed the presence of at least one complex pair on every branch even over R^+. The magnitude of the real parts is small as seen in table 4. Since grid refinement could be done only with the power iteration computation, that provided only the eigenvalue largest in magnitude. Even this computation on the finest grid used in the study revealed the largest eigenvalue on every branch to lie outside the unit circle. Hence we expect all solutions at $\lambda = 3 \times 10^6$ to be unstable. This is also consistent with our three-dimensional study (Ravi Sankar *et al.* 1991) where we have observed the development of a new form of streamwise periodic, three-dimensional flows at such high values of Gr.

5.3. *Effect of aspect ratio*

Since the aspect ratio is defined as $\gamma = b/a$, a value larger than unity implies that the shorter side of the duct is aligned parallel to the gravity vector (see figure 1). Thus for smaller-aspect-ratio ducts the two-cell flow structure remains the preferred one over a large range of λ while in larger-aspect-ratio ducts multicellular flows with the cells spanning the entire channel height such as those computed in Fung *et al.* (1987) are readily formed beyond a threshold value of λ. In the present study we restrict γ
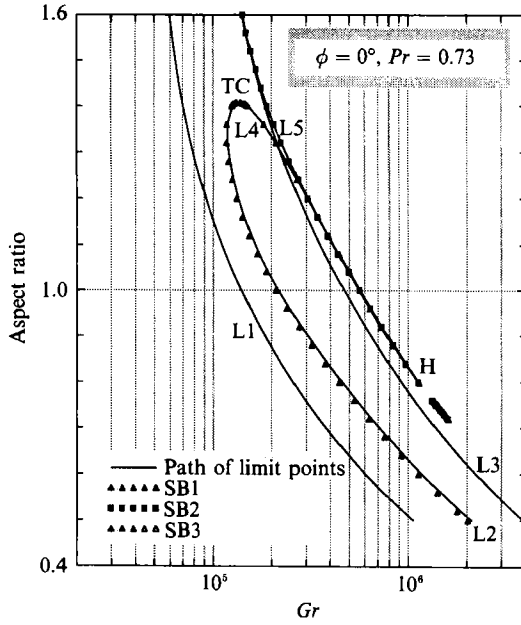
FIGURE 4. This figure shows how the various singular points found at $\gamma = 1.0$ and $Pr = 0.73$ are unfolded as the aspect ratio is changed. Limit points L2 and L4 come together at a transcritical point TC at $\gamma = 1.408$. With decreasing aspect ratio, L4 and L5 come together and disappear through a hysteresis point H at $\gamma = 0.791$. L2, L4 and L5 taken together can be seen to form a tilted cusp around H.
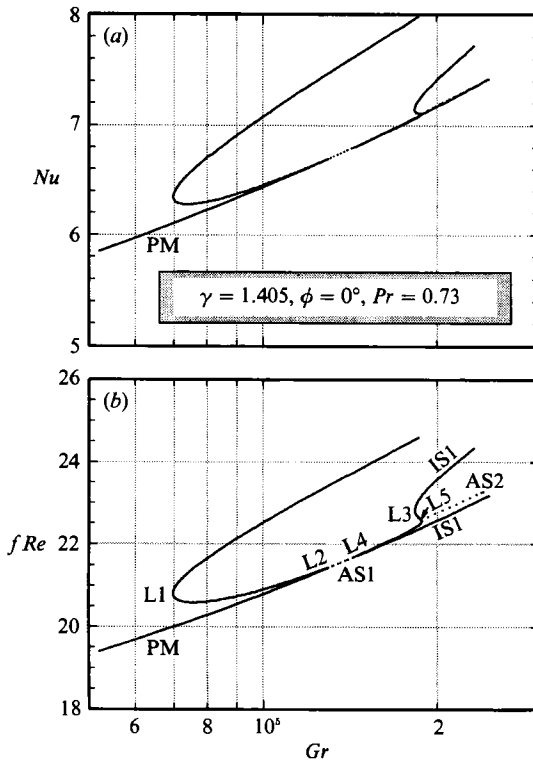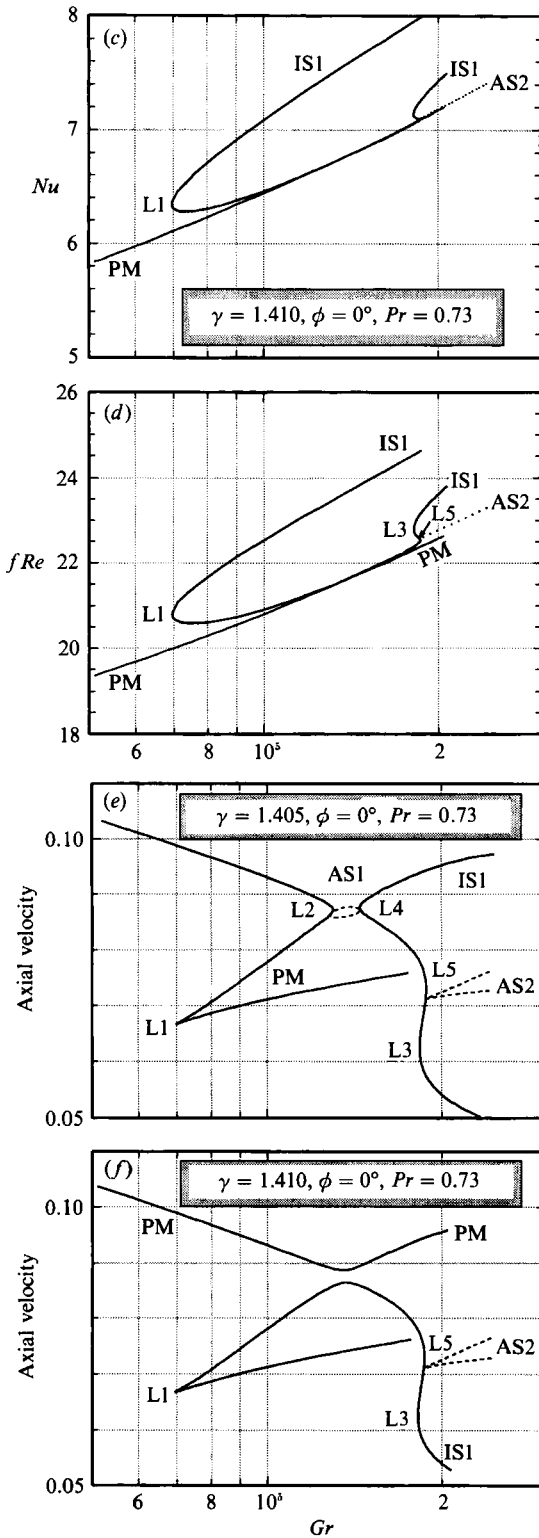

FIGURE 5 (a, b). For caption see facing page.

FIGURE 5. State diagrams show the solution structure for $Pr = 0.73$, $\phi = 0°$ just before ($\gamma = 1.405$) and after ($\gamma = 1.410$) the transcritical point. (a) Nu vs. Gr and (b) $f\,Re$ vs. Gr at $\gamma = 1.405$. (c) Nu vs. Gr and (d) $f\,Re$ vs. Gr at $\gamma = 1.410$. (e) Axial velocity at node $(2,2)$ vs. Gr at $\gamma = 1.405$. (f) Axial velocity at node $(2,2)$ vs. Gr at $\gamma = 1.410$. The changes in connectivity of the solution branches past the transcritical points are seen best in (e) and (f).
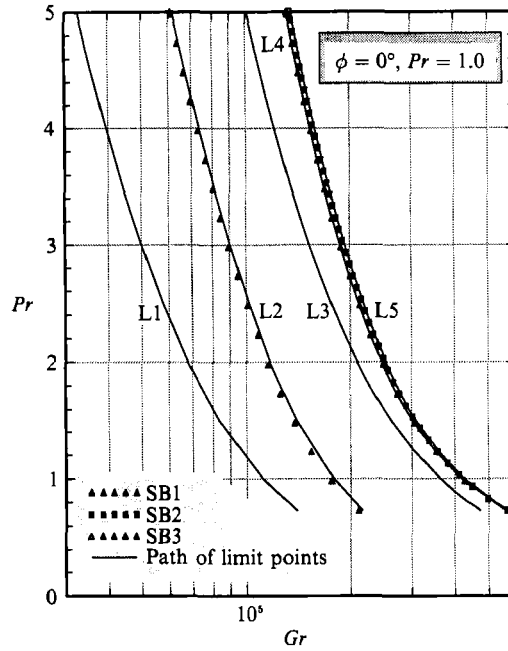
FIGURE 6. This figure shows how the various singular points found at $\gamma = 1.0$, $\phi = 0°$ and $Pr = 0.73$ are unfolded as the Prandtl number is changed. No higher-order singularities are present on these fold curves over a Pr range of 0.73 to 5.0.

to a range of 0.5 to 1.6. Figure 4 shows the unfolding of the singular points computed at $\gamma = 1$ as the aspect ratio is varied over this range at fixed values of $Pr = 0.73$ and $\phi = 0°$. The first fold curve corresponding to L1 demarcates the uniqueness region. As expected, the uniqueness region, where the two-cell flow prevails, increases with decreasing aspect ratio.

The changing aspect ratio can be regarded as a perturbation on the square geometry that preserves the reflective symmetry about the y-axis. Hence the symmetry-breaking bifurcation points (indicated by data points) remain robust to such perturbations. In particular SB1 and L2 continue to remain close to each other as γ is varied. Similar behaviour has been observed in both the Dean (Winters 1987) and Taylor (Cliffe & Mullin 1985) problems. The limit points L2 and L4 approach each other as the aspect ratio is increased and join at a turning point at $\gamma = 1.408$. This point, labelled TC in figure 4, can be viewed as either a limit point on the fold curve or as a transcritical point with respect to γ. Note that the two points L2 and L4 are on two different symmetric branches PM and IS1, respectively. An asymmetric branch AS1 connects these two branches as already seen in figure 2 (c, d). Thus the two symmetry-breaking points SB1 and SB2, that are near L2 and L4 respectively also come close to each other as the aspect ratio is decreased and coalesce near $\gamma = 1.408$. The state diagrams just before ($\gamma = 1.405$) and after ($\gamma = 1.410$) the transcritical point are shown in figure 5 (a–f). The limit points L2 and L4 can be seen to approach each other in figure 5 (a, b, e) and the asymmetric branch AS1 remains a closed loop, but shrinks in size. The change in connectivity between the branches PM and IS1 is quite evident in figure 5 (c, d, f). As in the Dean problem, the part of the branch IS1 that has a two-cell flow structure at $\gamma = 1.405$ becomes connected to the part of the branch PM originating at $\lambda = 0$. The two types of four-cell flows that are found on
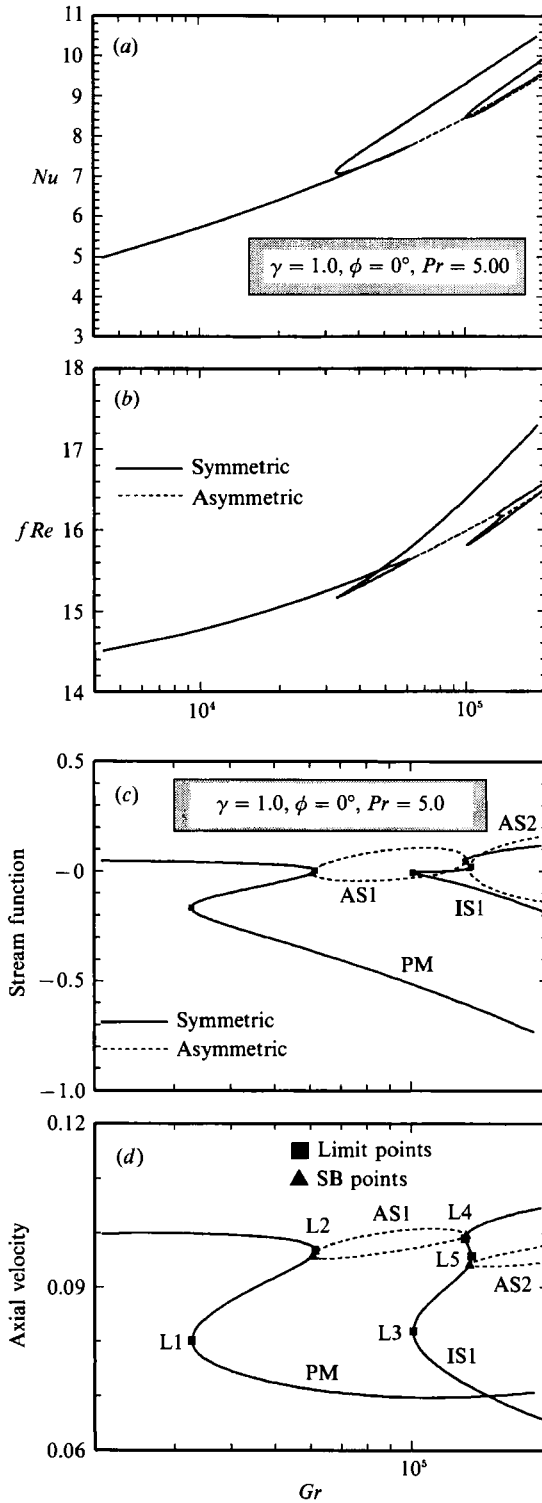
FIGURE 7. State diagram shows the solution structure for $\gamma = 1.0$, $\phi = 0°$, $Pr = 5.0$. (a) Nusselt number *vs. Gr*, (b) *fRe vs. Gr*, (c) stream function at node $(2, 2)$ *vs. Gr* and (d) axial velocity at node $(2, 2)$ *vs. Gr*. The solution structure remains essentially the same as found for $Pr = 0.73$.

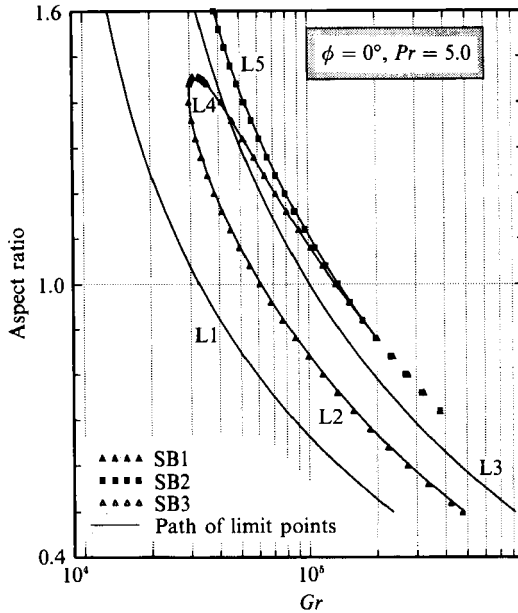FIGURE 8. This figure shows how the various singular points found at $\gamma = 1.0$, $\phi = 0°$, and $Pr = 5.0$ are unfolded as the aspect ratio is changed. As for $Pr = 0.73$ limit points L2 and L4 come together at a transcritical point at $\gamma = 1.456$. With decreasing aspect ratio, L4 and L5 come together and disappear through a hysteresis point at $\gamma = 0.719$.

different branches (point 3 on PM and point 2 on IS1) before the transcritical point are to be found on the same branch after the transcritical point. This branch is now isolated from the origin and disconnected.

Since the uniqueness region becomes enlarged with decreasing aspect ratio, the multiplicity features are found to occur at higher λ. All the singular points found at $\gamma = 1$ continue to be present up to $\gamma = 0.5$ with the exception of L4 and L5 and the symmetry-breaking points associated with them. These two limit points, which are on the isolated branch IS1, disappear through a hysteresis point at $\gamma = 0.791$. Viewing this point as the organizing centre, the fold curves L5, L4 and L2 can be interpreted as forming a tilted cusp with a transcritical point appearing on the fold curves L2, L4. The primary mode exchange process that takes place here is between two-cell flows lying on two different branches PM, IS1. By analogy with Taylor flows one would expect L5 to lead to another tilted cusp pointed in the opposite direction at higher aspect ratios that would form the basis of another primary mode exchange process between a two- and a four-cell flow.

5.4. *Effect of Prandtl number*

The effect of Pr on the solution structure is examined in figures 6–8. The singular points found at $\gamma = 1.0, Pr = 0.73$, $\phi = 0°$ are tracked as the Pr is changed from 0.73 to 5.0. Such fold curves are shown in figure 6. No higher-order singularities are found on these fold curves, indicating that the solutions structure remains the same for all Pr in this range. But the flow transitions take place at a much earlier Gr as Pr is increased. This observation is similar to the one made in (I) for flow through circular ducts. A larger value of Pr implies a smaller value of thermal diffusivity in comparison to the momentum diffusivity. Hence the thermal boundary layers are

FIGURE 9. State diagram shows how the solution structure unfolds when the channel cross-section is tilted slightly by $\phi = 1°$ for $Pr = 0.73$, $\gamma = 1.0$. (a) Nu vs. Gr and (b) fRe vs. Gr. (c, d) Axial velocity at node (2, 2) vs. Gr for $\phi = +1°$ and $\phi = -1°$ respectively. Note, that the SB points and the neighbouring limit points L2, L4 and L5 that were present in figure 2 have disappeared. In (c, d) the change in connectivity between the various branches for positive and negative tilts is shown.

thinner and the temperature in the interior becomes more uniform with increasing *Pr*. Hence the secondary flow which is driven by the horizontal temperature gradient is also weakened in the interior with increasing *Pr*.

The state diagrams for $\gamma = 1.0$, $Pr = 5.0$ are shown in figure 7 (*a–d*). Note that in figure 7 (*b*), the primary branch of *fRe vs. Gr* appears to intersect between limit points L1 and L2. But this is not a bifurcation point. The solution structure is once again best illustrated with the stream function and axial velocity at $(0.133, 0.133)$ as state functions as shown in figure 7 (*c, d*). The true singular points are indicated in these figures. The stability picture remains essentially the same as for $Pr = 0.73$ with the following exception. On the two-cell part of the branch IS1, the complex pairs with positive real parts appeared and disappeared sporadically as λ was varied continuously. This was monitored with the power iteration on the 29×14 grid. It is interesting that in the Dean problem Winters (1987) finds this part of the branch to be stable. In the case of $Pr = 0.73$ a complex pair appeared very near L4 and persisted on the entire branch, leading us to conclude that branch to be unstable for $Pr = 0.73$ in an oscillatory fashion. The situation is not so clear for $Pr = 5.0$.

Figure 8 shows the variation of the singular points with aspect ratio for $Pr = 5.0$. This structure also remains the same as for $Pr = 0.73$ with a transcritical point TC at $\gamma = 1.457$ and a hysteresis point H at $\gamma = 0.88$. The tilted cusp structure formed by L2, L4 and L5 is much more clearly visible in this figure. The symmetry-breaking bifurcation points are also robust with respect to changes in the Prandtl number as one would expect. They also remain close to the limit points. The only exception is their presence beyond the hysteresis point at which L4 and L5 disappear.

5.5. *Effect of tilt*

Stretching a square duct into a rectangle preserves the reflective symmetry in the problem. Hence the symmetry-breaking points found earlier remain structurally stable to such geometrical perturbations. In contrast tilting the duct, even slightly, destroys this symmetry. The symmetry-breaking points found in the earlier sections are structurally unstable to such geometrical perturbations and result in the smooth unfolding of the solution branches. In this section, the unfolding process at SB1, which takes place in the range of $0 < \phi < 0.15°$ is examined and the complete solution structure emerging for an imperfection of $\phi = 1°$ tilt is calculated for λ up to 7×10^6 ($Pr = 0.73$). Figure 9 shows the state diagram for this case at $\gamma = 1.0$, $Pr = 0.73$. Note that solutions for negative tilt can be constructed from those of positive tilt using (14). The macroscopic quantities such as Nu, fRe do not change for the same degree of positive or negative tilt. They are shown in figure 9 (*a, b*). The variation of the axial velocity at the point $(0.133, 0.133)$ with *Gr* is shown in figures 9 (*c*) and 9 (*d*) for positive and negative tilts, respectively. There are only three branches and the primary branch PM, which originates at $Gr = 0$, continues smoothly. The other two branches are disconnected and each has a simple limit point. These limit points correspond to L1 and L3 in the untilted case and they do remain even under a large degree of tilt.

Next we describe the unfolding process at SB1 for non-zero positive tilt. The behaviour is quite similar at other SB points. As ϕ increases from zero, the unfolding of SB1 changes the bifurcation diagram of figure 2 (*d*) into what is sketched in figure 10 (*a*). SB1 has unfolded into a limit point L2′ close to L2. With increasing ϕ, these two limit points coalesce into a hysteresis point (double limit point) at a critical angle $\phi*$; therefore they have disappeared for $\phi > \phi*$. We have calculated L2 and L2′ as
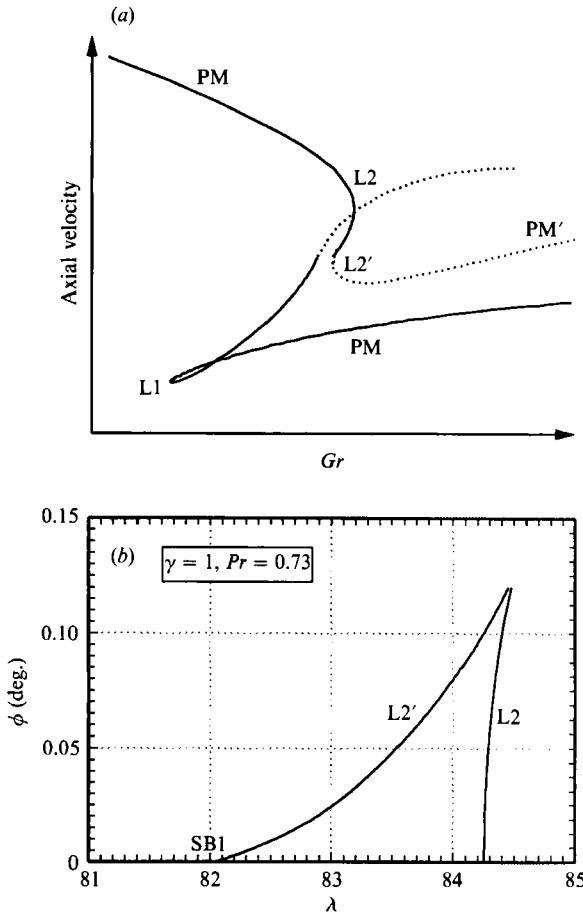
FIGURE 10. Unfolding of SB1 for $\gamma = 1$, $Pr = 0.73$. (a) Sketch of the state diagram near L2 for small tilt angles. The dashed curve corresponds to AS1 branch in figure 2(d). (b) Computed fold curve showing the variation of L2 and L2′ as a function of ϕ.

functions of ϕ, the result is shown in figure 10(b). Clearly, near $\phi = 0.12$, L2 and L2′ merge into a hysteresis point near $\lambda = 84.479$.

There may be further singular points on the folds shown in figure 10(b). When the primary branch PM in figure 10(a) passes through L2 and L2′, the number of positive eigenvalues changes from 0 to 1 to 2 making the part PM′ unstable. In fact, our eigenvalue calculations for tilt $\phi = 1°$ show that the branch PM leading to point 4 in figure 9(c) becomes unstable past a point where L2 was in the untilted case. But the instability is due to a pair of complex eigenvalues with positive real parts. One possible explanation of this behaviour is that there is an origin of a Hopf point (Takens–Bogdanov singularity) on the L2 fold in figure 10(b), from which a branch of Hopf points emerges. Hence, more complex interactions are apparently required to explain the evolution of the bifurcation diagram of figure 2 with respect to tilt. But the study of such effects is beyond the scope of the present paper.

There are still five different solutions at $Gr = 10^6$ and the terminal points in figure 9(c, d) are numbered 1–5. The flow profiles corresponding to these points are labelled and shown in figure 11(a–o). Figure 11(a–c) shows the flow profiles for positive tilt corresponding to point 4 in figure 9(c). The primary branch evolves continuously
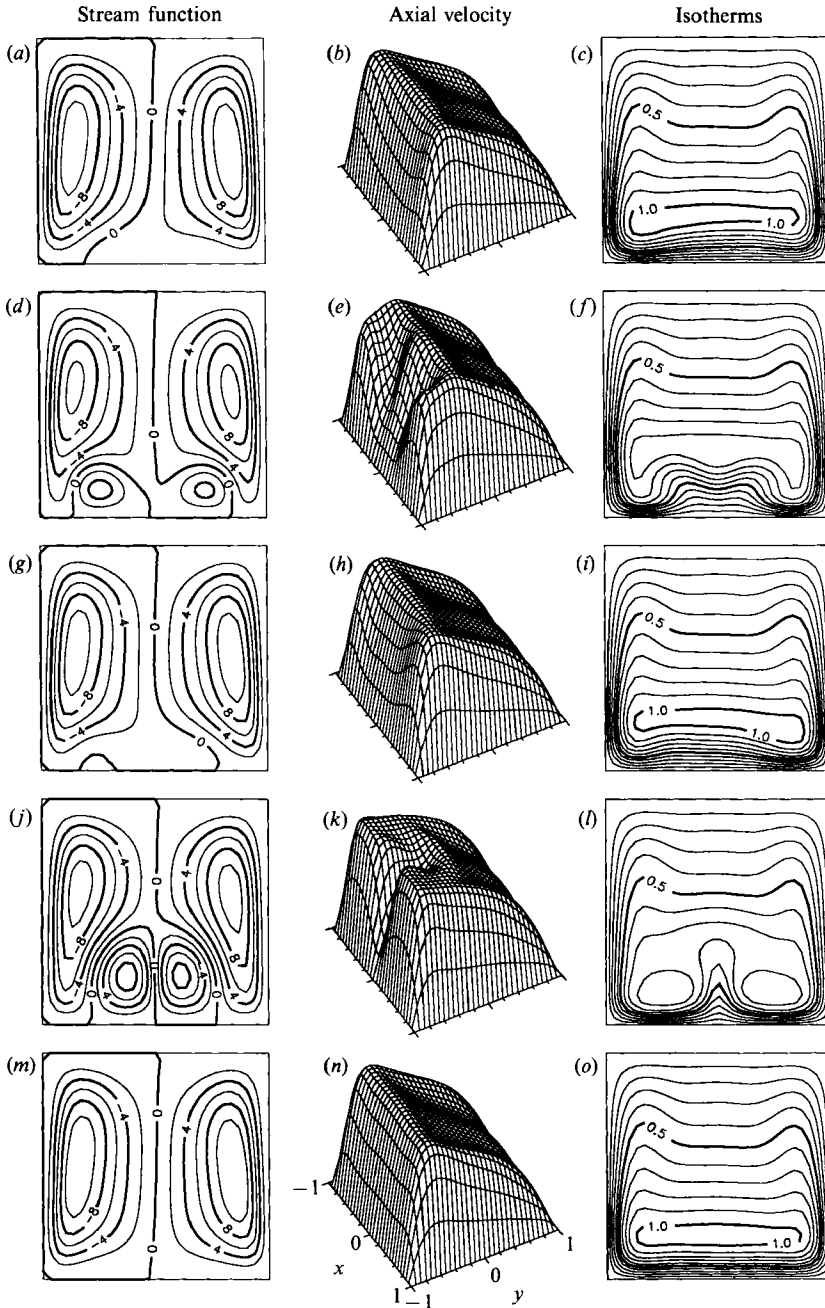
Stream function   Axial velocity   Isotherms

FIGURE 11. Five solutions are present at $\lambda = 3 \times 10^6$ and $Pr = 0.73$, $\gamma = 1.0$, $\phi = 1°$. These are labelled as points 1 to 5 in figure 9(c). (a) Streamline contours, (b) axial velocity perspective plots and (c) isotherm contours are shown for a two-cell pattern which lies on the branch PM (point 4). (d–f) Similar profiles for a four-cell pattern on the branch IS2 (point 2). (g–i) A two-cell pattern on the branch IS2 (point 5). (j–l) A four-cell solution on the branch IS1 (point 3). (m–o) A two-cell pattern on branch IS1 (point 1).
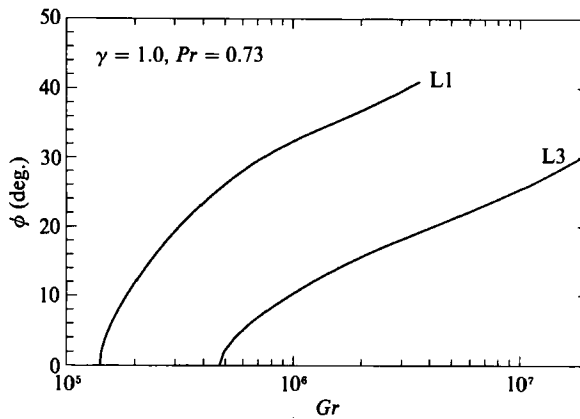
FIGURE 12. Variation of limit points L1 and L3 with tilt angle for $\gamma = 1.0$, $Pr = 0.73$.

from the origin $\lambda = 0$ to point 4. For a positive tilt, even in the uniqueness region corresponding to small values of λ, the separating streamline moves towards the left. Viewing the tilt to be around the lower left corner, this is to be expected as increasing the tilt to 45° should cause the separating line to reach the lower left corner, thus once again establishing a symmetry about the vertical line. Hence movement of the separating streamline towards the left corner at the bottom wall is regarded as the natural flow for positive tilt. Note that near the SB point corresponding to zero tilt, the primary branch unfolds, selecting that part of the asymmetric branch which corresponds to the natural flow. Thus if the tilt is negative, the primary branch will select the alternative path as seen in figure 9(*d*). At the same λ, however, another two-cell flow exists with the separating streamline shifted to the right as in figure 11(*g*–*i*). This is an anomalous flow and lies on the disconnected branch IS2 corresponding to point 5. As expected the primary branch would evolve towards this point for negative tilt (figure 9*d*). The four-cell flows found at zero tilt are also present for small non-zero tilt, but they are situated on the isolated branches as secondary modes. These are shown in figure 11(*d*–*f*) for point 2 and in figure 11(*j*–*l*) for point 3.

The fold curve tracing the variation of these limit points with tilt angle is shown in figure 12. Note that these limit points move to larger values of Grashof numbers with increasing tilts. Thus with increasing tilt, the two-cell flow remains the only solution over a larger range of Gr.

6. Conclusions

The multiplicity features of two-dimensional mixed-convection flows through a rectangular duct are studied. The bifurcation structure is determined for a square duct for $Pr = 0.73$ and 5.0. Up to five different solutions are found within a Gr range of 0–10^6. Three of the branches located in this range of Gr are new. Determination of the linear stability of these solutions indicates that all of them develop one or other mode of instability. In particular the four-cell flow is found to be unstable to asymmetric perturbations. While time-periodic branches may emerge through Hopf bifurcation, they are believed to be physically unrealizable. The most likely possibility is the development of streamwise periodic, three-dimensional flows which

break the translational symmetry that has been assumed in the present work. A study of such three-dimensional flows will be reported in follow-up work.

For $Pr = 0.73$ five limit points and three symmetry-breaking points have been computed over a Grashof number range of 0 to 10^6 for a square duct. Additional limit points appear at higher Gr. Since all the known two-dimensional solutions become unstable even at $Gr = 10^6$, the solution structure at higher Gr has not been determined. The variation of these singular points with the aspect ratio has been determined using the fold-following algorithm. A transcritical point is found at $\gamma = 1.408$ and a hysteresis point is found at $\gamma = 0.791$. Upon tilting the duct even slightly (1°), the symmetry-breaking points unfold to yield smooth solution branches. The solution structure remains unchanged as Pr is increased. The singular points, however, occur at lower values of Gr as Pr is increased.

REFERENCES

ALLEN, M. B., HERRERA, I. & PINDER, G. F. 1988 *Numerical Modeling in Science and Engineering.* John Wiley.

BENJAMIN, T. B. 1978 Bifurcation phenomena in steady flows of a viscous fluid, I. Theory. *Proc. R. Soc. Lond.* A **359**, 1–26.

CHENG, K. C. & HWANG, G.-J. 1969 Numerical solution for combined free and forced laminar convection in horizontal rectangular channels. *Trans. ASME* C: *J. Heat Transfer* **91**, 59–66.

CHENG, K. C. & YUEN, F. P. 1987 Flow visualization studies on secondary flow patterns in straight tubes downstream of a 180° bend and in isothermally heated horizontal tubes. *Trans. ASME* C: *J. Heat Transfer* **109**, 49–54.

CHOU, F. C. & HWANG, G.-J. 1984 Combined free and forced laminar convection in horizontal rectangular channels for high Re-Ra. *Can. J. Chem. Engng* **62**, 830–836.

CHU, E., GEORGE, A., LIU, J. & NG, E. 1984 SPARSPAK. *Research Rep.* CS-84-36. Dept. of Computer Science, University of Waterloo.

CLIFFE, K. A. & MULLIN, T. 1985 A numerical and experimental study of anomalous modes in the Taylor experiment. *J. Fluid Mech.* **153**, 243–258.

DEAN, W. R. 1927 The stream-line motion of fluid in a curved pipe. *Phil. Mag.* **5**, 673–695.

DENNIS, S. C. R. & NG, M. 1982 Dual solutions for steady laminar flow through a curved tube. *Q. J. Mech. Appl. Maths* **35**, 305–324.

FARIS, G. N. & VISKANTA, R. 1969 An analysis of combined forced and free convection heat transfer in a horizontal tube. *Intl J. Heat Mass Transfer* **12**, 1295–1309.

FUNG, L., NANDAKUMAR, K. & MASLIYAH, J. H. 1987 Bifurcation phenomena and cellular-pattern evolution in mixed-convection heat transfer. *J. Fluid Mech.* **177**, 339–357.

HOLGER, W. W. 1988 *Applied Numerical Linear Algebra.* Prentice Hall.

HWANG, G.-J. & CHENG, K. C. 1970 Boundary vorticity method for convective heat transfer with secondary flow – applications to the combined free and forced convection in horizontal tubes. *Heat Transfer* **4**, Paper NC3.5.

IQBAL, M. & STACHIEWICZ, J. W. 1966 Influence of tube orientation on combined free and forced laminar convection heat transfer. *Trans. ASME* C: *J. Heat Transfer* **88**, 109–116.

JEPSON, A. & SPENCE, A. 1985 Folds in solutions of two parameter systems and their calculations. Part I. *SIAM J. Numer. Anal.* **22**, 347–368.

KELLER, H. B. 1977 *Applications of Bifurcation Theory* (ed. P. H. Rabinowitz), p. 359. Academic.

MOORE, G. & SPENCE, A. 1980 The calculation of turning points of non-linear equations. *SIAM J. Numer. Anal.* **17**, 567–576.

MORTON, B. R. 1959 Laminar convection in uniformly heated horizontal pipes at low Rayleigh numbers. *Q. J. Mech. Appl. Maths* **12**, 410–420.

NANDAKUMAR, K. & MASLIYAH, J. H. 1982 Bifurcation in steady laminar flow through curved tubes. *J. Fluid Mech.* **119**, 475–490.

NANDAKUMAR, K., MASLIYAH, J. H. & LAW, H. S. 1985 Bifurcation in steady laminar mixed convection flow in horizontal ducts. *J. Fluid Mech.* **152**, 145–161 (referred to herein as I).

PATANKAR, S. V., RAMADHYANI, S. & SPARROW, E. M. 1978 Effect of circumferentially nonuniform heating on laminar combined convection in a horizontal tube. *Trans. ASME* C: *J. Heat Transfer* **100**, 63–70.

RAVI SANKAR, S., NANDAKUMAR, K. & MASLIYAH, J. H. 1988 Oscillatory flows in coiled square ducts. *Phys. Fluids* **31**, 1348–1359.

RAVI SANKAR, S., NANDAKUMAR, K. & WEINITSCHKE, H. J. 1991 Mixed convection heat transfer in horizontal ducts. Part 2: Development of three-dimensional, streamwise periodic flows. *J. Fluid Mech.* (to be submitted).

ROACHE, P. J. 1972 *Computational Fluid Dynamics*. Hermosa.

SHAH, R. K. & LONDON, A. L. 1978 *Laminar Flow Forced Convection in Ducts*. Academic.

SPENCE, A. & WERNER, B. 1982 Non-simple turning points and cusps. *IMA J. Numer. Anal.* **2**, 413–427.

VAN DYKE, M. 1990 Extended Stokes series: laminar flow through a heated horizontal pipe. *J. Fluid Mech.* **212**, 289–308.

WEINITSCHKE, H. J. 1985 On the calculation of limit and bifurcation points in stability problems of elastic shells. *Intl J. Solids Structures* **21**, 79–95.

WEINITSCHKE, H. J., NANDAKUMAR, K. & RAVI SANKAR, S. 1990 A bifurcation study of convective heat transfer in porous media. *Phys. Fluids* A **2**, 912–921.

WERNER, B. & SPENCE, A. 1984 The computation of symmetry breaking bifurcation points. *SIAM J. Numer. Anal.* **21**, 388–399.

WINTERS, K. H. 1987 A bifurcation study of laminar flow in a curved tube of rectangular cross-section. *J. Fluid Mech.* **180**, 343–369.

YANG, Z.-H. & KELLER, H. B. 1986*a* Multiple laminar flows through curved pipes. *Appl. Numer. Maths.* **2**, 257–271.

YANG, Z.-H. & KELLER, H. B. 1986*b* A direct method for computing higher order folds. *SIAM J. Sci. Statist. Comput.* **7**, 351–361.